Radiation Measurements 193 (2026) 107631

Contents lists available at ScienceDirect

Radiation Measurements

journal homepage: www.elsevier.com/locate/radmeas

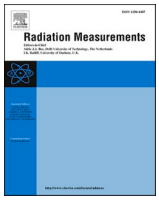

Design of a collimator-free SPECT system based on multi-layer grid scintillator array

Xue Yang [a], Changran Geng [a,b,*], Lu Han [a], Feng Tian [c], Ningxin Dong [a], Xiaobin Tang [a,b,**]

[a] Department of Nuclear Science and Technology, Nanjing University of Aeronautics and Astronautics, Nanjing, 210016, People's Republic of China
[b] Key Laboratory of Advanced Nuclear Technology and Radiation Protection, Ministry of Industry and Information Technology, Nanjing, 210016, People's Republic of China
[c] Department of Nuclear Medicine, Jiangsu Province Hospital, The First Affiliated Hospital with Nanjing Medical University, Nanjing, 210029, People's Republic of China

ARTICLE INFO

Keywords:
Collimator-free SPECT
Grid scintillator array
Spatial resolution
Detection efficiency

ABSTRACT

Traditional single-photon emission computed tomography (SPECT) systems exhibit a tradeoff between spatial resolution and sensitivity because of the use of mechanical collimators. To address this issue, this paper proposes a collimator-free SPECT detector design based on a staggered multilayer grid scintillator array, to enable image reconstruction without requiring conventional mechanical collimation. Based on the experimental and simulation results, the system parameters were evaluated and a practical configuration incorporating 25 mm-long elongated scintillators, 6 mm-thick grid layers, and 40 mm layer spacing was established. To preliminarily assess the clinical-scale system performance, a clinical-scale system featuring a 15-detector annular array with a 300 mm rotation radius was simulated to emulate realistic cardiac SPECT imaging conditions. The results demonstrated that the system had a 0.76% detection efficiency on a clinical scale (compared to 0.1% for conventional SPECT), successfully resolving point sources spaced 2 mm apart. The cylinder model imaging results demonstrated that the mean activity recovery coefficient (ARC) of the reconstructed images for each cylinder was between 0.5 and 0.6. This preliminary result validates the feasibility of a collimator-free SPECT system and lays the foundation for further improvements in reconstruction accuracy. The proposed approach offers a potentially viable solution for concurrently enhancing spatial resolution and detection sensitivity in SPECT systems, with promising applications in myocardial perfusion imaging.

1. Introduction

Coronary artery disease (CAD) is one of the leading causes of mortality worldwide, accounting for approximately 17.8 million deaths annually (Brown et al., 2023). Ischemic heart disease (IHD), the predominant pathological manifestation of CAD, poses a significant threat to human health. Myocardial perfusion imaging (MPI) has emerged as a vital diagnostic modality for CAD evaluation because of its noninvasive nature and functional assessment capabilities. As a principal MPI technique, single-photon emission computed tomography (SPECT) myocardial perfusion imaging has become the gold standard for CAD diagnosis in developed nations owing to its distinctive diagnostic merits. SPECT MPI demonstrates an average sensitivity of 86% and a specificity of 74% in detecting coronary artery stenosis with greater than 50% probability (Gheisari et al., 2025), providing critical evidence for risk stratification and therapeutic decision-making in CAD patients. According to the 2024 National Nuclear Medicine Status Survey results, cardiovascular imaging accounted for 4.6% of SPECT imaging in China in 2023 (Wang et al., 2025). Although this percentage is low, cardiovascular imaging still plays an irreplaceable role in clinical practice because of its unique value in diagnosing and assessing the prognosis of coronary heart disease.

Traditional dual-probe SPECT systems typically employ thallium-doped sodium iodide (NaI(Tl)) scintillator crystal detectors coupled with parallel-hole collimators. However, these systems can only achieve a spatial resolution of 10-15 mm and a detection efficiency of 0.01-0.02% due to the physical limitations of parallel-hole collimators (Chua

* Corresponding author. Department of Nuclear Science and Technology, Nanjing University of Aeronautics and Astronautics, Nanjing, 210016, People's Republic of China.
** Corresponding author. Department of Nuclear Science and Technology, Nanjing University of Aeronautics and Astronautics, Nanjing, 210016, People's Republic of China.
E-mail addresses: gengchr@nuaa.edu.cn (C. Geng), tangxiaobin@nuaa.edu.cn (X. Tang).

https://doi.org/10.1016/j.radmeas.2026.107631
Received 24 August 2025; Received in revised form 1 February 2026; Accepted 2 February 2026
Available online 3 February 2026

et al., 2006). This limits their use in myocardial perfusion imaging applications. To overcome these technical constraints, next-generation dedicated cardiac SPECT systems utilize multi-pinhole collimators and cadmium zinc telluride (CZT) semiconductor detector technology (Bocher et al., 2010; Dorbala et al., 2018; Erlandsson et al., 2009; Hutton et al., 2018), substantially improving system performance and enhancing the spatial resolution to 5 - 8 mm. Representative products include Spectrum Dynamics D-SPECT and GE Discovery NM 530c systems (Ma et al., 2023). Although CZT detectors dramatically improve the imaging quality, their high manufacturing costs hinder their widespread adoption.

Additionally, conventional SPECT systems rely on mechanical collimators for spatial resolution, which have inherent design limitations. Collimators create an irreconcilable tradeoff between system sensitivity and spatial resolution, such that improving spatial resolution requires reducing the collimator aperture size, which substantially diminishes system sensitivity; conversely, increasing the aperture size enhances sensitivity at the expense of degraded spatial resolution. Current data indicate that the majority of contemporary cardiac SPECT systems have detection efficiencies ranging from 0.01 to 0.1% with spatial resolution exceeding 5 mm (Patton et al., 2007; Slomka et al., 2014). To address this issue, Ma et al. (2021) proposed the self-collimation concept. This concept replaces part of the physical collimator with spatially distributed sensitive detectors, thereby improving the sensitivity and spatial resolution of the system.

Inspired by the self-collimation principle, this manuscript proposes a collimator-free SPECT detector. A feasibility study was conducted to assess its potential in clinical applications. The investigation focused primarily on validating its capability for three-dimensional imaging while also examining the influence of key structural parameters on detection efficiency and spatial resolution.

2. Materials and methods

2.1. System architecture

The proposed system incorporates a multilayer grid architecture comprising orthogonally oriented elongated scintillators. Successive layers are laterally offset, producing layer-specific variations in the photon detection profiles, thereby enabling collimator-free imaging. Pronounced layer-specific variations in photon detection profiles requires ensuring that the grid layers have an appropriate thickness while incorporating a densely arranged scintillator array with an adequate thickness behind the final grid layer. The thickness of this array should exceed that of the preceding grid layers to ensure that the system maintains sufficient detection efficiency. Notably, an excessive thickness of the anterior grid modules results in significant photon absorption, substantially diminishing the detectable photon flux in subsequent modules and degrading the layer-specific variations in photon detection profiles.

For a proof-of-concept evaluation, a six-module detector assembly was designed (Fig. 1a and b). For the first five modules, a grid configuration (Fig. 1c) was adopted, whereby adjacent scintillator layers were displaced laterally by 1 mm. Each grid module consists of two parts: the first part features three sets of scintillators arranged horizontally at equal intervals, with 5 mm spacing between adjacent sets; the second part comprises three sets of scintillators arranged vertically at the same intervals, thereby forming an orthogonal grid structure with air gaps. The sixth module consists of a densely packed array of 25 scintillators per layer, arranged side by side without any gaps, and the total number of layers is determined based on the scintillator thickness optimization results described in Section 3.1. Additionally, the modules maintain a specific vertical spacing, and the cross-sectional dimensions of single scintillator are 1 mm × 1 mm.

Notably, an excessive thickness of the anterior grid modules results

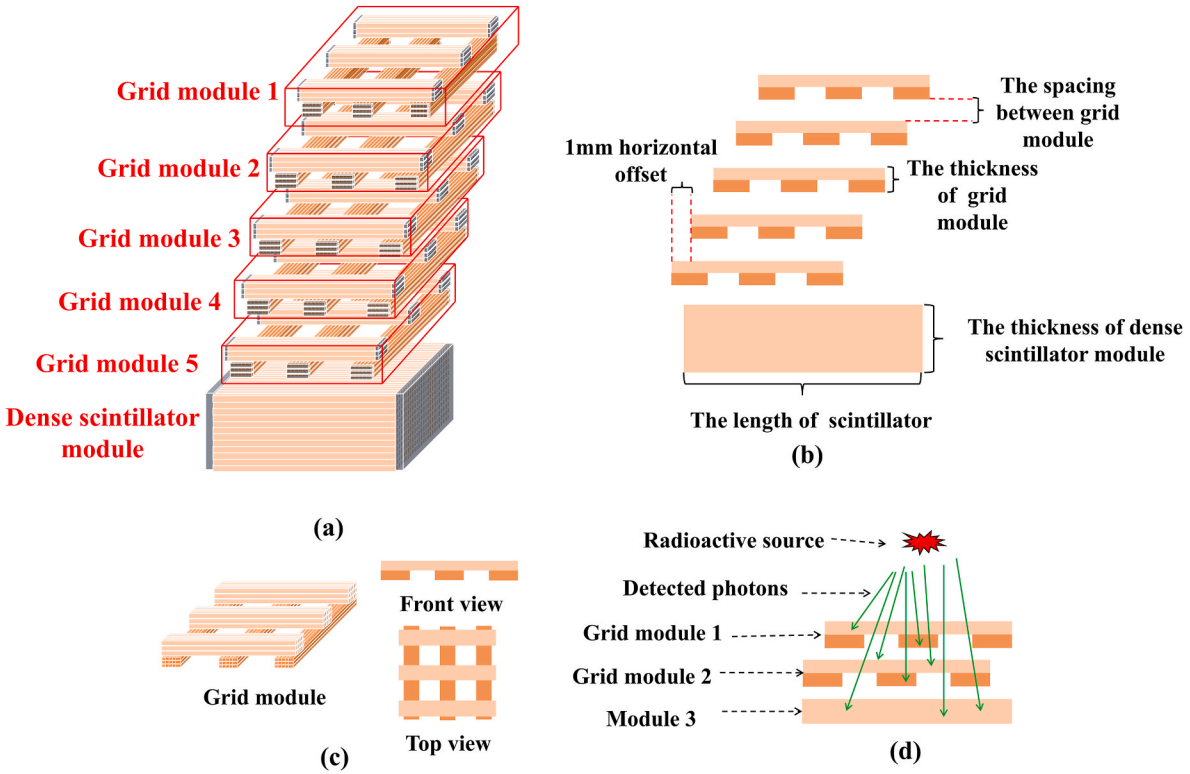

Fig. 1. (a) Three-dimensional schematic of the collimator-free SPECT detector architecture. (b) Front view of the collimator-free SPECT detector architecture with the optimized parameters annotated. (c) Schematic diagram of grid structure. (d) Schematic diagram of photon detection, with two grid modules shown for illustrative purposes.

in significant photon absorption, substantially diminishing the detectable photon flux in subsequent modules and degrading the layer-specific variations in photon detection profiles.

Unlike conventional SPECT systems, this configuration eliminates the need for mechanical collimators, allowing photon counts from all detector positions to contribute to the reconstruction (Fig. 1d). Spatially resolved photon counts within a single detection plane exhibit characteristic variations because of the transverse misalignment of the grid layers, particularly in Modules 1 and 2.

Based on the aforementioned principles, the system architecture constructed within the GEANT4 Monte Carlo toolkit (version 11.0.2) (Agostinelli et al., 2003; Allison et al., 2006, 2016) is illustrated in Fig. S1 (Supplementary material). A circular structure comprising fifteen detectors was established to record events with deposited energies ranging from 137 to 140 keV. During subsequent data processing, a Gaussian broadening was applied to the deposited energy values. The physics list employed in the simulations was QGSP_BERT, with all electromagnetic production cuts and transport thresholds kept at the default values provided by Geant4. This study did not activate optical processes, focusing primarily on key physical interactions such as photoelectric effects and Compton scattering of gamma rays within the detectors. Given that the study emphasizes the detector configuration, external factors such as the walls, floor, bed, and human models in the actual clinical environment, were not incorporated into the simulation.

2.2. Imaging principle

Images were formed by constructing a system response matrix that accurately modeled these spatial variations, followed by an iterative reconstruction using the maximum-likelihood expectation–maximization (MLEM) algorithm. The MLEM algorithm formula (Lange and Carson, 1984) is provided in Eq (1):

$$\bar{f}_j^{(k+1)} = \frac{\bar{f}_j^{k}}{\sum_{i=1}^{n} a_{ij}} \sum_{i=1}^{n} \frac{g_i}{\sum_{j'=1}^{m} a_{ij} \bar{f}_{j'}^{(k)}} a_{ij} \tag{1}$$

where a_{ij} denotes the probability that a photon emitted from pixel j is detected by pixel i, and g_i denotes detection t pixel i, where $\bar{f}^{(0)}$ can be either a homogeneous value or a value obtained by a simple back-projection (SBP) algorithm. In this study, an analytical modeling method (Yu et al., 2016) was used to calculate a_{ij} (Fig. S2 (Supplementary material)), and the formula is given by Eq (2) as follows:

$$a_{ij} = \frac{\Omega_{ij}}{4\pi} * e^{-\int_{L_s}^{L_e} \mu(l) dl} \tag{2}$$

where, j denotes a pixel in the imaging space, and i denotes a pixel in the detector space. L_s represents the center position of a pixel in the imaging space, while L_e represents the center position of a pixel in the detector space. μ is the linear attenuation coefficient of the material for photons at a given energy. a_{ij} indicates the probability that pixel j in the imaging space is detected by pixel i in the detector space. Ω_{ij} denotes the solid angle subtended by imaging space pixel j relative to detector space pixel i.

The MLEM iterative algorithm used in this study requires at least 350 iterations. To further demonstrate that this number of iterations is necessary for convergence, the sum of absolute differences between the reconstruction results of the current iteration and the previous iteration across all pixels, ΔV_j in Eq (3), is computed(Goulet et al., 2013).

$$\Delta V_j = \sum_i \left| V_i^j - V_i^{j-1} \right| \tag{3}$$

where i the pixel number in the reconstructed image, j is the iteration number. The stopping criterion employed in this work was either (1) ΔV reaches a plateau (i.e., it does not decrease with further iterations), or (2) ΔV reaches a value below 0.05. Fig. S3 (Supplementary material) also presents the variation of ΔV with the number of iterations in this study. also presents the variation of ΔV with the number of iterations in this study.

2.3. Geometrical optimization of the detector system

According to Section 2.1, the geometric parameters that must be determined for the detector architecture designed in this study are the thickness of each module, length of the scintillator, and spacing between neighboring grid layers. Among these, the thickness of the grid layers and the spacing between adjacent grid layers are determined through computational simulation, while the scintillator length is established based on experimental measurements.

The thickness of each module was determined by analyzing the photon attenuation characteristics of lutetium yttrium oxyorthosilicate (LYSO), for γ-ray energies of 140, 364, and 511 keV, using data from the National Institute of Standards and Technology (NIST). LYSO scintillators offer notable advantages, including high density, high light output, and non-hygroscopicity (Nakanishi et al., 2017). Furthermore, based on the attenuation characteristics, the thickness of the entire detector can be determined, which in turn can be used to determine the thickness of each module.

The superior detection performance of LYSO supports reliable measurements using a single elongated scintillator. Therefore, the elongated scintillator length was determined by comparing the energy resolution across different lengths of LYSO (Epic Crystal Company) in the experimental measurements. As shown in Fig. 2a, the scintillators had lengths of 20, 25, 40 mm, and end surfaces of 1×1 mm^2. All scintillators were wrapped with 0.2 – 0.5 mm $BaSO_4$ reflective layers and featured optically polished end surfaces.

The experimental setup, illustrated in Fig. 2b, utilized a dual-ended readout configuration. NDL EQR15-11-3030D-S Silicon Photomultipliers (SiPMs; Novel Device Laboratory, Beijing, China), featuring an active area of 3.0×3.0 mm^2, were optically coupled to the polished ends of single scintillator bar. The resulting analog signals were digitized using a four-channel data acquisition module (TOFTEK DAQBOX-4-125M). Energy resolution was characterized using a ^{99m}Tc source (20 – 24 μCi) placed at various positions along the scintillator (Fig. 2c). Data were acquired for 15 s at each position, yielding count rates between approximately 1.0×10^4 and 1.5×10^4 counts per second (cps). Each trigger event recorded a timestamp and two integrated energy values; these data were subsequently used to reconstruct the energy spectra and calculate energy resolution.

To determine the spacing between neighboring grid layers in the detector, different grid-layer spacings (30, 40, 50, and 60 mm) were configured to evaluate the imaging performance of various structures. Two types of point source distributions were simulated: (1) A dual-point source model, consisting of two point sources spaced 2 mm and 3 mm apart, was used to assess the system's resolution capability for closely positioned sources. (2) A three-point source model was employed to simulate complex multisource distributions, and the three point sources were distributed at right angles, with 3 mm of spacing between neighboring sources. For both configurations, a total of 8×10^9 particles were simulated, with identical activity assigned to each source.

2.4. Data processing and performance evaluation

In this study, contrast-to-noise ratio (CNR) was used to evaluate the performance of the point source reconstruction results, and the ARC was used to evaluate the effectiveness of the system on the cylinder-model reconstruction results. The Figure of Merit (FOM) is used to evaluate the spatial resolution and reconstruction accuracy of the system.

The CNR is defined as the ratio of the signal intensity difference to noise level in an image (Hendrick and Hendee, 2008; Rodriguez-Molares et al., 2020) and is calculated as follows:

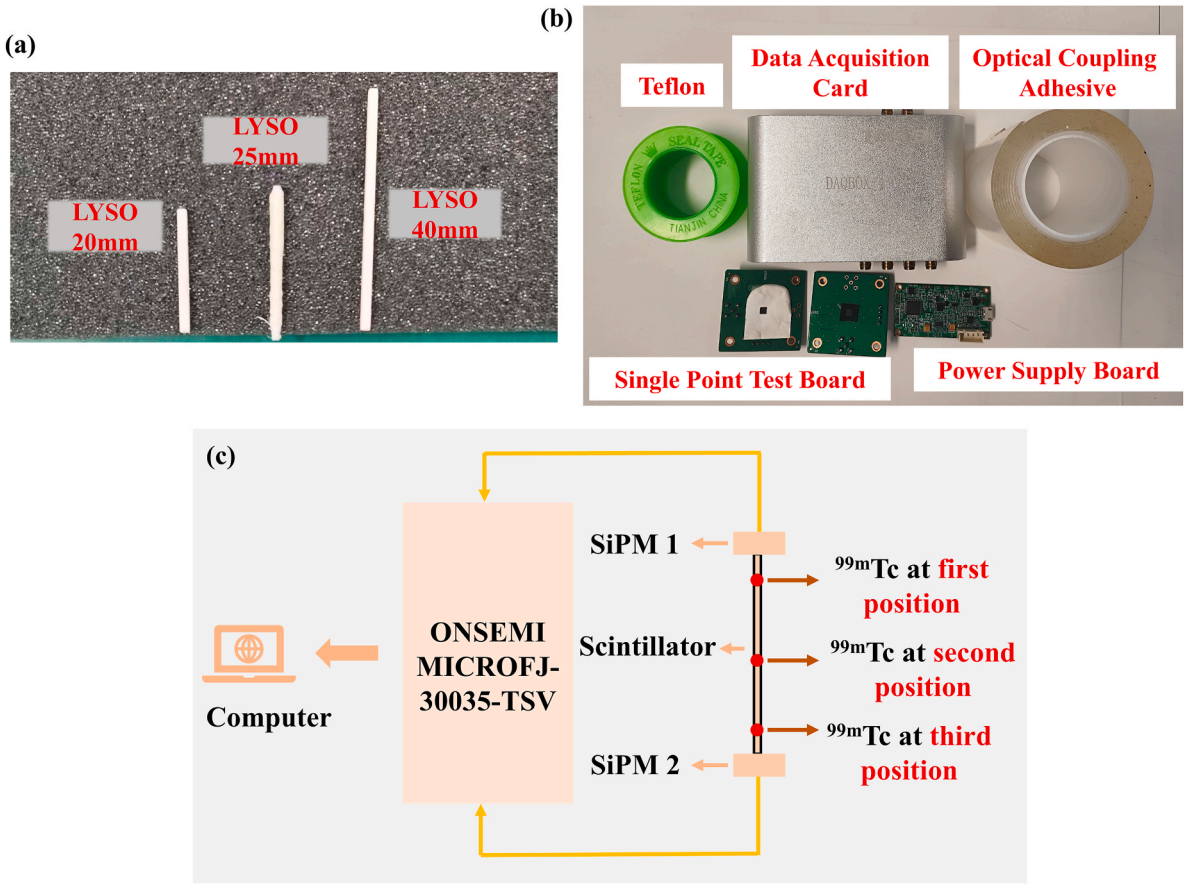

Fig. 2. (a) LYSO scintillators with lengths of 20, 25, and 40 mm and (b) Experimental equipment used in the experiment. (c) Experimental set-up for energy resolution measurements.

$$CNR = \frac{|\mu_i - \mu_{bk}|}{\sigma} \tag{4}$$

where μ_i denotes the mean value of the pixels in the region of interest (ROI); μ_{bk} denotes the mean value of the pixels in the background region; and σ denotes the standard deviation of the background region. The ROI did not include pixels at the edge positions near the radioactive source, whereas the background region included edge pixels and pixels in other nonradioactive regions.

The ARC is defined as the ratio of the reconstructed to the true activity value (Leube et al., 2024; Vergnaud et al., 2023), calculated as follows:

$$ARC = \frac{A_{reconstruction}}{A_{true}} \tag{5}$$

where $A_{reconstruction}$ represents the total reconstructed activity within the region of interest (ROI), and A_{true} represents the true activity. In this study, the reconstructed activity was obtained by multiplying the image pixel values by a calibration factor derived from point source reconstructions performed under identical geometric and acquisition conditions as the cylinder models. For each point source, the calibration factor was calculated as the ratio of its preset true activity to the sum of pixel values in its ROI. The final calibration factor used in this study, derived from averaging the calibration factors calculated from multiple point source reconstruction results, is 0.74. Based on this calibration relationship, the reconstructed activity estimate was calculated by summing pixel values within the ROI in the reconstructed image. This value was then compared with the true activity set in the simulation to determine the ARC for the reconstructed image.

The FOM is defined as the ratio of the center-to-center distance between the two reconstructed sources to the sum of their full widths at half maximum (FWHMs) (Zhai and Li, 2019), expressed by the formula:

$$FOM = \frac{d_{cc}}{FWHM_1 + FWHM_2} \tag{6}$$

where, d_{cc} is the center-to-center distance between the two reconstructed sources, while $FWHM_1$ and $FWHM_2$ denote the full width at half maximum of source 1 and source 2, respectively.

Furthermore, the energy resolution (ER) is often expressed as a percentage and evaluated using the following formula (Gunaratna Mudiyanselage et al., 2024), which is also adopted in this study for calculating the energy resolution.

$$\mathrm{ER} = \frac{FWHM}{E_{peak}} \tag{7}$$

where E_{peak} is the energy of the photopeak.

3. Results

3.1. Impact of the thickness of each module

As shown in Fig. 3a, the LYSO scintillations exhibited significant attenuation characteristics for gamma rays at 140, 364, and 511 keV. Due to its high density, the attenuation efficiency for γ-rays at these energies exceeds 90% when the thickness reaches 40 mm. Further thickness increases did not result in a significant improvement in γ-ray attenuation; therefore, the overall thickness of the system structure was set to 40 mm. As discussed in Section 2.1, a grid module with consistent thickness enhances the layer-specific photon detection profiles;

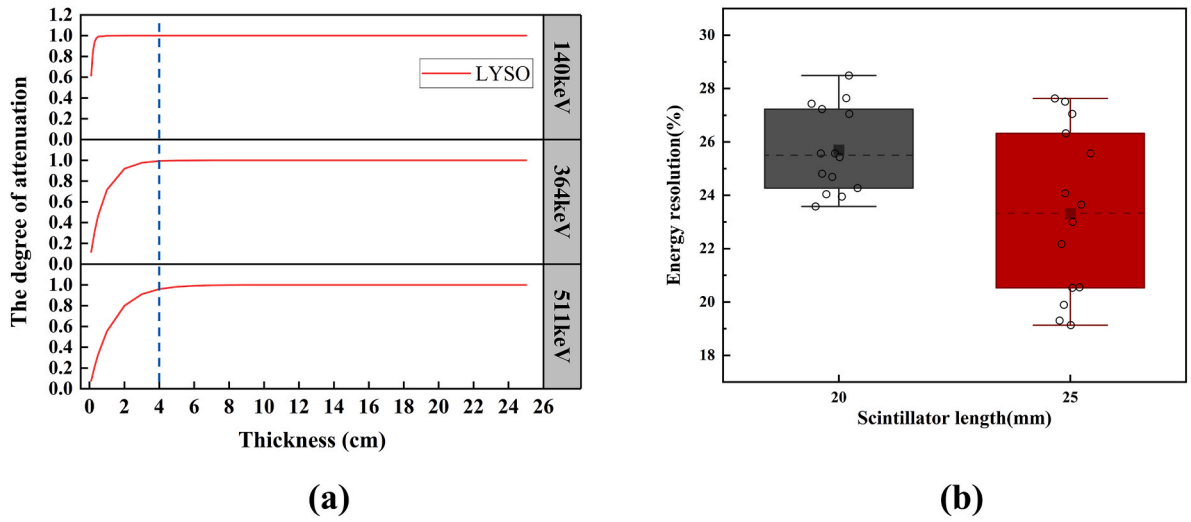

Fig. 3. (a) Attenuation characteristics of the LYSO scintillator at different energies. (b) Energy resolution results of ^{99m}Tc source irradiation at different position of LYSO scintillators.

however, the thickness must remain moderate to avoid compromising the overall performance. The total thickness of the system architecture was 40 mm and comprised five grid-layer modules and one dense scintillator array module. Accordingly, each grid-layer module was assigned a thickness of 6 mm, and the thickness of the sixth module was set to 10 mm.

3.2. Impact of scintillator length

Fig. 3b presents the measured energy resolution of the LYSO scintillator, utilizing a ^{99m}Tc source, across various irradiation positions. Systematic measurements were limited to the 20 mm and 25 mm scintillators. For the 40 mm length, measurable photopeak were absent in the acquired spectra (Fig. S4 (Supplementary material)), which is

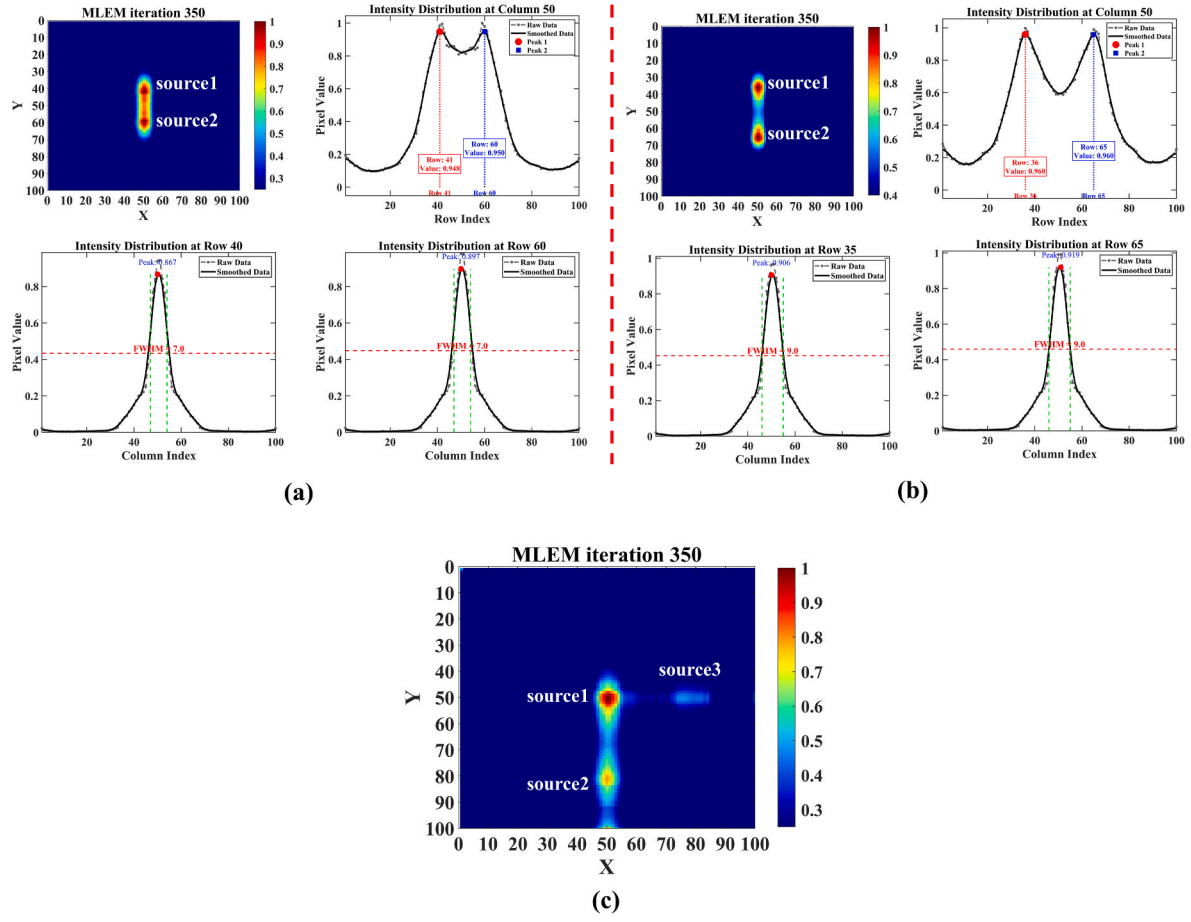

Fig. 4. Reconstructed images of point sources under a layer spacing of 60 mm. (a) two point sources 2 mm separation; (b) two point sources 3 mm separation; (c) three point sources, with the distance between each adjacent pair of points being 3 mm.

attributed to severe optical attenuation over the longer path leading to critically low effective photoelectron counts at the SiPMs. The measurement results indicate that the difference in energy resolution between the two scintillator lengths is relatively small, with the average energy resolution for the 20 mm scintillator being 25.69% and that for the 25 mm scintillator being 23.31%. These results are generally consistent with the performance levels reported in existing studies (Nakanishi et al., 2017; Wei et al., 2020). Based on the energy resolution results and considering the effective detection area requirements in the current detector design, adopting a 25 mm long scintillator allows for a larger detection area while maintaining comparable energy resolution performance. Therefore, after comprehensive evaluation, a scintillator length of 25 mm was ultimately selected for this study.

3.3. Impact of grid layer spacing

The reconstruction results (Fig. S5–S7 (Supplementary material)) indicate that increasing the inter-layer spacing of the grid contributes to improved imaging quality. Fig. 4 shows the reconstruction results of three configurations of point sources under a layer spacing of 60 mm. In the three-point-source model, despite identical activity settings for all sources, the reconstructed activity estimate for the centrally located source 1 appeared significantly higher, a phenomenon primarily attributable to reconstruction artifacts. In contrast, the weaker recovery observed for source 2 and source 3, positioned at the edge of the imaging field, resulted from degraded geometric sensitivity and incomplete projection data, exacerbated for source 3 by its spatial offset from the axis of rotation. Source 2, aligned with the rotation axis, maintained relatively superior data integrity, leading to better reconstruction performance compared to source 3.

Quantitative analysis further substantiates the aforementioned trend. For the dual-point source with a 3 mm separation (Fig. 5b), as the layer spacing increases from 30 mm to 60 mm, the CNR of source 1 and source 2 improves from 3.92 and 4.23 to 6.42 and 6.54, respectively. Concurrently, the average FWHM decreased from 1.78 (±0.05) mm to 0.90 (±0.04) mm, and the average FOM increased from 0.86 (±0.01) to 1.66 (±0.08) (Table 1).

In the more demanding case of 2 mm-spaced point sources, enlarging the layer spacing similarly led to pronounced enhancements in imaging performance: the CNR values of two sources rose from 4.41 and 4.63 to 6.83 and 7.03 (Fig. 5a), the average FWHM was reduced from 1.77 (±0.05)mm to 0.78(±0.05)mm, and the average FOM improved substantially from 0.57(±0.01) to 1.33(±0.08) (Table 2). Consistent with these results, the three-point-source model exhibited the same tendency, with the CNR of all sources showing progressive improvement as the spacing was widened (Fig. 5c).

Overall, increasing the detector spacing improved the significance of the counting difference and optimized the spatial resolution. For 140 keV gamma rays, a spacing of at least 40 mm is required to achieve a higher spatial resolution.

Table 1
FWHM and FOM for dual-point sources with 3 mm separation.

Spacing	Source 1 (FWHM/mm)	Standard Error	Source 2 (FWHM/mm)	Standard Error	FOM	Standard Error
30 mm	1.78	0.05	1.73	0.05	0.86	0.01
40 mm	1.35	0.03	1.38	0.05	1.10	0.03
50 mm	1.15	0.07	1.17	0.05	1.29	0.04
60 mm	0.90	0.04	0.93	0.05	1.66	0.08

Table 2
FWHM and FOM for dual-point sources with 2 mm separation.

Spacing	Source 1 (FWHM/mm)	Standard Error	Source 2 (FWHM/mm)	Standard Error	FOM	Standard Error
30 mm	1.77	0.05	1.75	0.06	0.57	0.01
40 mm	1.40	0.04	1.32	0.05	0.73	0.01
50 mm	1.15	0.05	1.17	0.05	0.86	0.02
60 mm	0.78	0.05	0.75	0.05	1.33	0.08

3.4. Preliminary evaluation in coronary artery disease imaging

A 15-detector circular array with a 300-mm rotation radius was constructed to evaluate the applicability of the system in clinical cardiac SPECT scenarios (Fig. 6). The grid-layer spacing in the detectors was set to 40 mm.

In the simulations, only the geometric setup is simulated, and a human model is not included in the simulation. The simulation objects consist of two categories: point sources and cylinder models. For point source simulations, two spatial distributions were configured: one with dual point sources spaced 2 mm apart, and another with dual point sources spaced 3 mm apart. For cylinder model simulations, two geometric configurations were established: the first is a dual-cylinder model with a center-to-center distance of 10 mm between the two cylinders; the second is a four-cylinder model, in which the vertical center spacing between adjacent cylinders is 10 mm and the horizontal center spacing is 14 mm. All cylinders share identical dimensions, with a length of 10 mm along the x-axis and a radius of 2 mm. The total number of emitted particles in all the above simulations was set to 8×10^9.

At the clinical geometric scale, the system can clearly distinguish point sources separated by 2 mm and 5 mm, demonstrating favorable spatial resolution. (Fig. 7a and b). The corresponding CNR are shown in Fig. 7c. All CNR values exceed 5, which is typically considered acceptable for routine image quality. Collectively, these results validate that the proposed collimator-free SPECT architecture can achieve effective radioisotope source imaging at clinically relevant dimensions.

The imaging results of the cylindrical models are shown in Fig. 8 (two cylinders) and Fig. 9 (four cylinders). Combined with the 3D reconstruction results (Fig. 8a and 9a), the shape of the cylinders can be preliminarily identified, though certain discrepancies remain compared

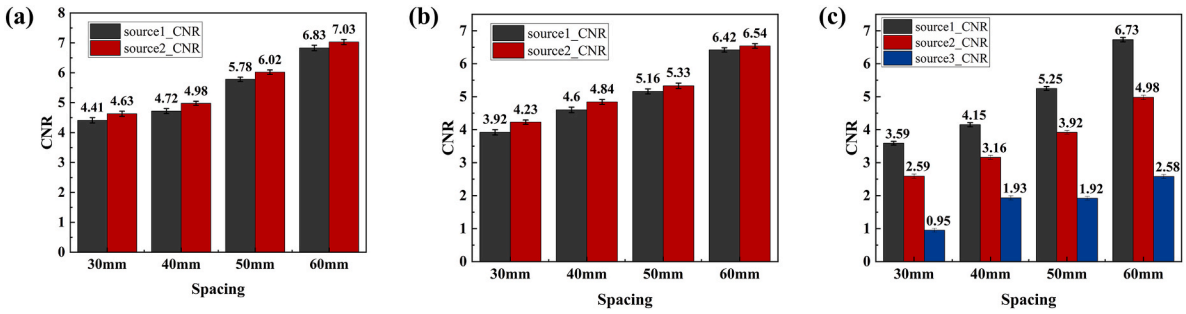

Fig. 5. CNR variations with error bars (representing standard error) for different source configurations: (a) dual-point sources with 2 mm separation, (b) dual-point sources with 3 mm separation, and (c) three-point sources.

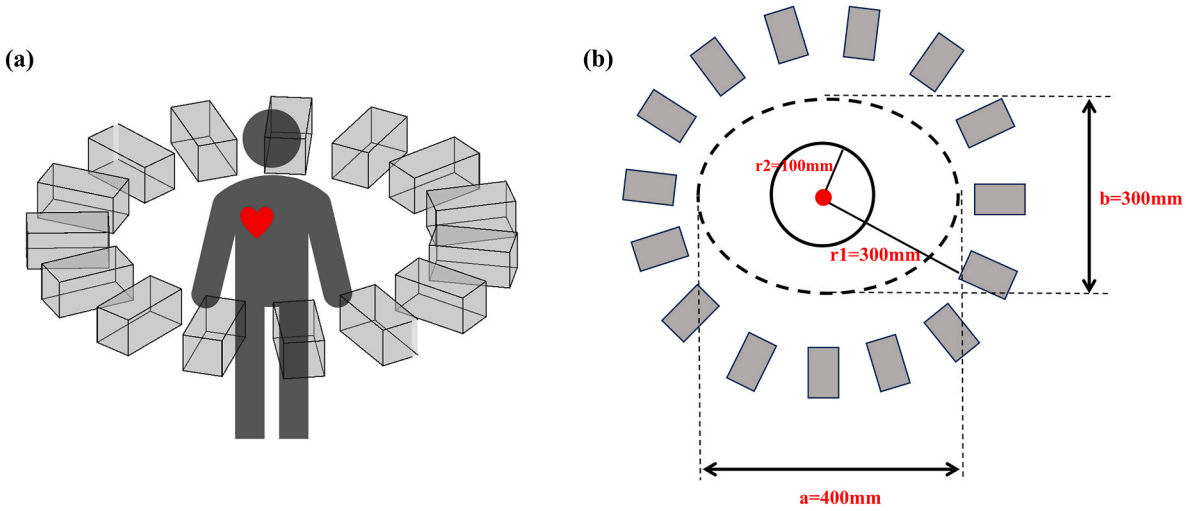

Fig. 6. Schematic of SPECT under clinical geometric conditions.

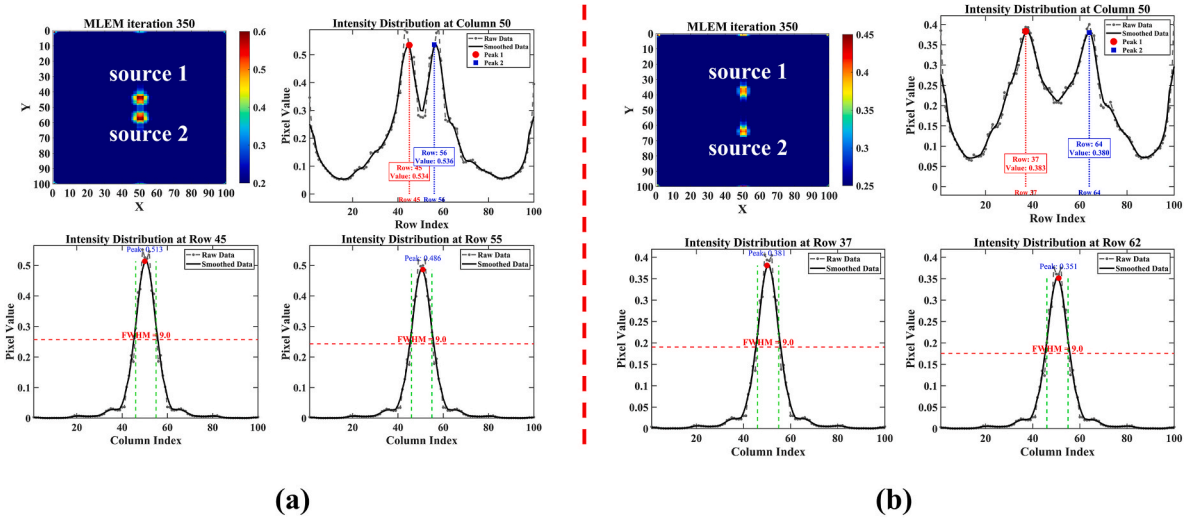

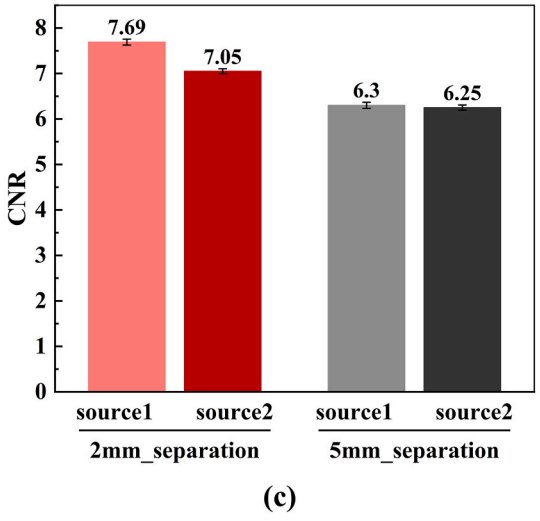

Fig. 7. Reconstruction results of dual-point source models with spacings of (a) 2 mm and (b) 5 mm. (c) CNR with error bars (representing standard error) for dual-point source models with 2 mm and 5 mm separation.

to their actual geometry. To further evaluate the reconstruction performance, cross-sectional visualizations along the three main axes

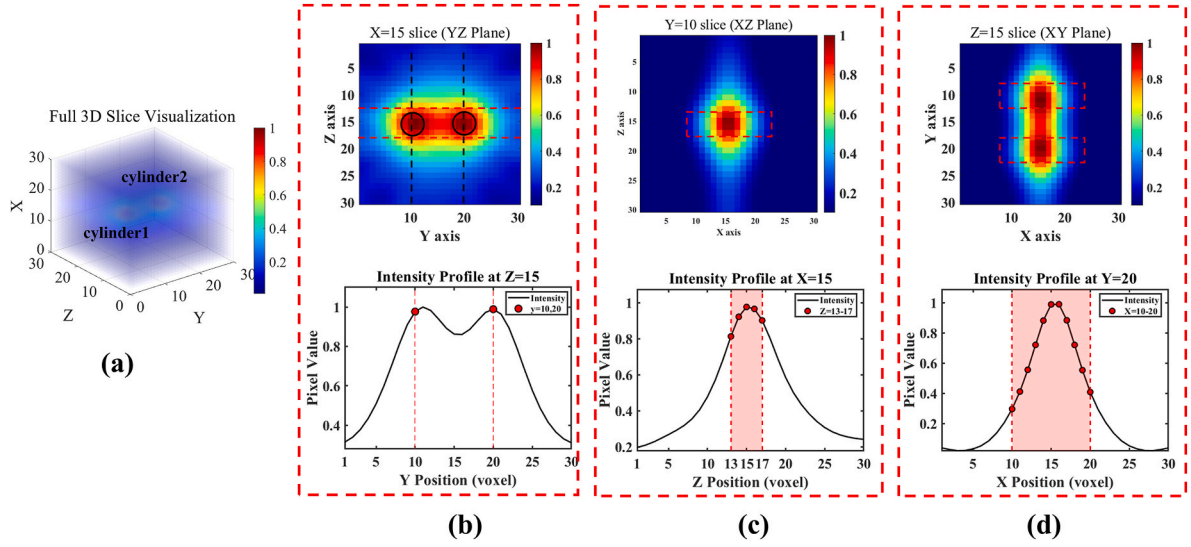

Fig. 8. Reconstruction results of the two-cylinder model: (a) three-dimensional reconstruction, (b) x-section, (c) y-section, (d) z-section.

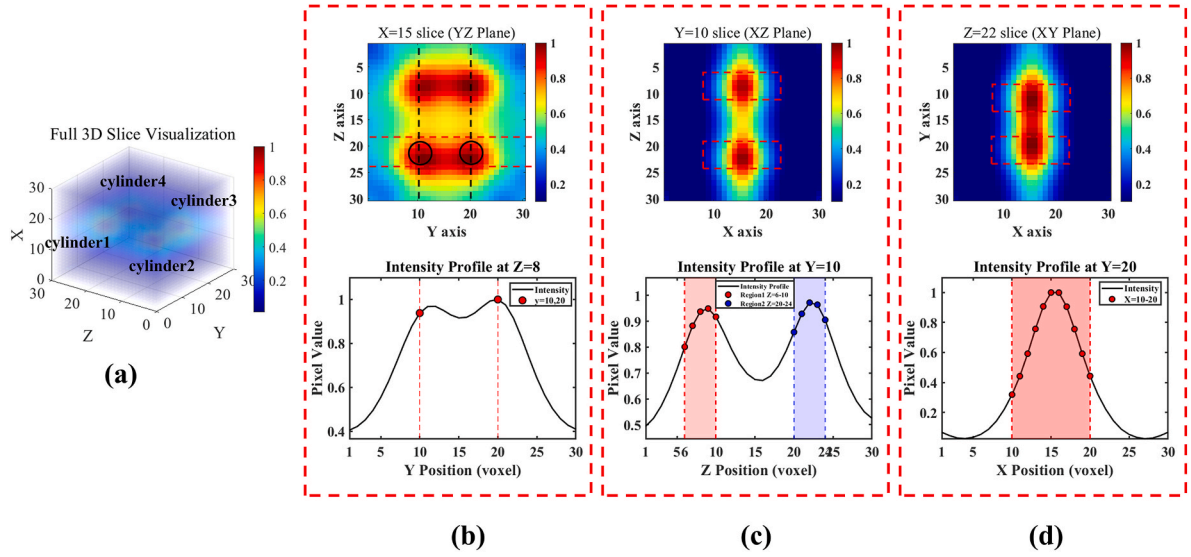

Fig. 9. Reconstruction results of the four-cylinder model: (a) three-dimensional reconstruction, (b) x-section, (c) y-section, (d) z-section.

were performed for both models, as presented in Figs. 8 and 9, where (b) denotes the x-section, (c) denotes the y-section, and (d) denotes the z-section. For the cylinder with a height of 10 mm along the x-axis, the center position in the x-section aligns closely with the actual location. For the cylinder with a height of 10 mm along the x-axis, the center position in the x-section largely matches the actual location. Furthermore, the ARC values of the cylinders shown in Fig. 10, ranging between 0.5 and 0.6, serve as preliminary evidence that validates the feasibility of reconstructing volumetric sources using the proposed collimator-free structure. Nevertheless, the reconstruction quality still requires further improvement.

Furthermore, on a clinical scale, this system demonstrates a detection efficiency of 0.76% (Table 3), representing an approximately 7.6-fold improvement over those of conventional SPECT systems ($\leq$0.1%).

4. Discussion

The study proposes a collimator-free SPECT structure with staggered multi-layer grid detector arrays. With this design, significant differences in the photon counts were detected by different grid detectors, which enabled the distribution of the radioactive source to be determined. Imaging results from the point source and cylinder models demonstrated that the proposed system can resolve point sources with 2-mm separation while achieving 0.76% sensitivity. These results verify the feasibility of the proposed collimator-free structure and demonstrate performance improvements to a certain extent compared to traditional SPECT. Compared with the self-collimating SPECT prototype developed by Tsinghua University (Ma et al., 2021), the present simulation results still show a gap in spatial resolution. The prototype system from Tsinghua University achieves a spatial resolution of 0.3 mm, which is attributed primarily to its implementation of combined translational and rotational motion of the imaging object. This methodology has been employed in several PET and SPECT studies. (Yan et al., 2013; Zeraatkar et al., 2020).

While the current system is capable of imaging three-dimensional structures, analysis across different cross-sections indicates that substantial room for improvement remains in reconstruction quality. In this study, all detectors rotate around a fixed axis—a design that exhibits certain limitations compared to existing dedicated cardiac SPECT systems such as the GE NM 530c and the Spectrum Dynamics D-SPECT

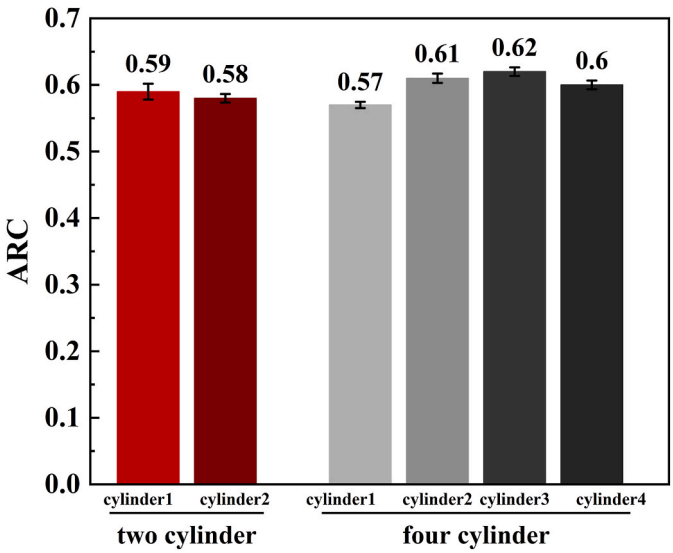

Fig. 10. ARC values with error bars (representing standard error) for the two-cylinder and four-cylinder models on a clinical scale.

Table 3
Detection efficiency of the system on a clinical scale.

	Two-cylinder model	Four-cylinder model
Number of particles emitted	8×10^9	8×10^9
Number of particles detected	61,045,070	61386028
Detection efficiency	0.76%	0.77%

(Nakano, 2016). In those systems, each detector can perform fan-beam scanning around its own axis, thereby acquiring multi-view data simultaneously from a single angular position. This configuration markedly improves imaging sensitivity and reconstruction accuracy, suggesting that significant potential still exists for optimizing multi-angle data acquisition and reconstruction algorithms in the present system. Subsequent research will focus on further optimizing the detector sampling strategy, such as translating the object being measured or shifting the rotation axis of the detector, to acquire more sampling information.

The calibration method used in this study for calculating the ARC provides a practical benchmark for the preliminary quantitative assessment of the reconstructed image quality. Future work will focus on enhancing the system's intrinsic quantitative accuracy by optimizing the reconstruction algorithm, such as developing more accurate system matrix models, accounting for photon scattering, and incorporating attenuation corrections. The ultimate goal is to reduce reliance on calibration factors.

Additionally, the simulations in this study were conducted under relatively idealized assumptions with a primary focus on the energy deposited in the scintillator and the assumption that the light output is proportional to the deposited energy. However, previous studies have experimentally and numerically investigated the impact of scintillation non-proportionality on detector performance (Breitenmoser et al., 2023; Cano-Ott et al., 1999; collaboration et al., 2024; Valentine and Rooney, 1994), and have reported that gadolinium aluminum gallium garnet (GAGG) scintillator exhibits good proportional response in the energy range from 260 keV to 435 keV (Kaewkhao et al., 2016). Given that this study focuses on the 140 keV energy, future research can build upon existing findings to further analyze the scintillation non-proportionality characteristics of LYSO scintillators in similar energy ranges and make appropriate corrections to simulation results.

In addition to the intrinsic response characteristics of the scintillator, simplifying the optical transmission and detection processes is another idealized assumption in this simulation. This consideration stems partly from computational cost concerns. As Nishikido et al. (2005) noted in their study, incorporating the generation, transmission, and detection of optical photons into the simulation would consume enormous computational resources. This simplification may somewhat overestimate certain system properties, such as detection efficiency, while neglecting the actual effects of optical interfaces. Future work will progressively incorporate optical transmission models during modular verification to more accurately assess system performance. On the other hand, the overarching objective of this study is to conduct a preliminary feasibility study. This simulation approach, which focuses on core detector components while simplifying the external environment, has precedents in SPECT-related simulation research (Chen et al., 2017; Dong et al., 2018; Feng et al., 2025; Van Audenhaege et al., 2013). For instance, numerous studies primarily evaluate collimator and detector performance without considering other complex factors. In practice, photon scattering and attenuation from surrounding environment do influence detector counting rates. Further investigation into these effects will be undertaken in subsequent research.

For the LYSO scintillator, its inherent background radiation does indeed exert a certain influence on the detection of 140 keV radiation. However, several existing studies on gamma camera simulation and development for SPECT applications have indicated that image contrast degradation due to LYSO's background counts is not critical for gamma cameras used in SPECT (Aguiar et al., 2012; Deprez et al., 2013; Liang et al., 2009; Lois et al., 2010). Consequently, the influence of background radiation will be systematically investigated and evaluated in subsequent prototype-stage experiments.

As outlined in Section 2.1 of this paper, the current findings are based on relatively idealized conditions, with the complete optical transport and electronics processes not being simulated. This approach was taken because the primary focus of the present work lies in the optimized design of the detector itself and in validating the feasibility of the proposed imaging concept. It should be noted that the performance evaluation in this study is based on idealized simulation conditions. In practical applications, errors introduced by low count rates and complex physical effects (such as scattering, attenuation, and statistical noise) will result in a decrease in system performance (e.g., ARC, CNR, spatial resolution) compared to the theoretical estimates reported here. In future prototype experiments, factors such as electronic noise, energy thresholds, signal pile-up, and dead-time effects will be incorporated to enable a more comprehensive evaluation of system performance.

For prototype validation, subsequent efforts will prioritize the following research directions: dual-ended SiPM readout and front-end electronics design; signal processing and calibration workflows (e.g., energy-spectrum normalization, peak-shift compensation, scatter correction); development of dedicated control and data-management software; and depth-of-interaction correction along with image-quality enhancement. These engineering and calibration-oriented studies will form the core of the next phase, aimed at advancing the imaging concept from proof-of-principle toward a realizable prototype system.

The collimator-free SPECT structure proposed in this study eliminates the need for a traditional mechanical collimator while retaining essential components such as the detector, photomultiplier tubes (PMTs), and back-end electronic systems (Celler and Spectrometry, 2010). Although this design removes the collimator section, the detector structure itself becomes more complex, which may lead to a certain increase in system cost. Nevertheless, this approach offers a feasible technical pathway for simultaneously improving system sensitivity and spatial imaging resolution. Compared to Compton cameras, which similarly require no mechanical collimator, the two designs differ in imaging mechanisms and applicable energy ranges. Compton cameras, based on electronic collimation principles, are typically suited for medium-to-high energy gamma-ray imaging (Roser et al., 2021). In contrast, the proposed structure is optimized primarily for low-energy gamma photons (e.g., 140 keV), demonstrating relatively better

imaging performance within this energy range. Furthermore, image reconstruction for Compton cameras is notably challenging due to the complexity of the algorithms involved (Kishimoto et al., 2017; Rigaud and Hahn, 2021). In comparison, the reconstruction method adopted in this study maintains reasonable imaging quality with reduced complexity, though further investigation is still needed to enhance algorithm robustness and computational efficiency. Certainly, both the collimator-free SPECT and the Compton camera are promising imaging technologies, which remain under active research and continuous optimization.

5. Conclusion

In this study, a mechanical collimator-free SPECT detector design is proposed. The implementation of a staggered multi-layer grid detector array configuration allowed the system to achieve a 2 mm spatial resolution and 0.76% detection efficiency at 140 keV photon energy, representing significant improvements over conventional SPECT systems. Through experiments and an optimized design, the use of a 25 mm-long inorganic scintillator and 40 mm layer spacing can substantially improve photon detection efficiency while ensuring good energy resolution. The activity distribution of the cylindrical mode was reconstructed in simulations. Compared to conventional SPECT, this design provides a solution that simultaneously improves spatial resolution and sensitivity and is expected to play an important role in the early diagnosis of coronary heart disease and efficacy assessments in the future.

CRediT authorship contribution statement

Xue Yang: Writing – original draft, Visualization, Validation, Methodology, Investigation, Conceptualization. **Changran Geng:** Writing – review & editing, Supervision, Methodology, Funding acquisition, Data curation. **Lu Han:** Writing – review & editing, Methodology. **Feng Tian:** Writing – review & editing, Methodology. **Ningxin Dong:** Writing – review & editing, Data curation. **Xiaobin Tang:** Writing – review & editing, Supervision, Project administration, Funding acquisition.

Ethics statement

The authors have nothing to report.

Declaration of competing interest

The authors declare that they have no known competing financial interests or personal relationships that could have appeared to influence the work reported in this paper.

Acknowledgements

This work is supported in part by the National Natural Science Foundation of China (Grant No. 12220101005), and the Foundation of Graduate Innovation Center in NUAA (Grant No. xcxjh20240624).

Appendix A. Supplementary data

Supplementary data to this article can be found online at https://doi.org/10.1016/j.radmeas.2026.107631.

Data availability

The data that support the findings of this study are available from the corresponding author upon reasonable request.

References

Agostinelli, S., Allison, J., Amako, K., Apostolakis, J., Araujo, H., Arce, P., Zschiesche, D., 2003. GEANT4-a simulation toolkit. Nucl. Instrum. Methods Phys. Res. 506 (3), 250–303. https://doi.org/10.1016/s0168-9002(03)01368-8.

Aguiar, P., Iglesias, A., Couce, B., Lois, C., 2012. A feasibility study on the use of arrays of discrete SiPMs for MR compatible LYSO readout using Monte Carlo simulation. J. J. o. I. J. Instrum. 7 (6), P06002. https://doi.org/10.1088/1748-0221/7/06/P06002.

Allison, J., Amako, K., Apostolakis, J., Araujo, H., Dubois, P.A., Asai, M., Yoshida, H., 2006. Geant4 developments and applications. IEEE Trans. Nucl. Sci. 53 (1), 270–278. https://doi.org/10.1109/tns.2006.869826.

Allison, J., Amako, K., Apostolakis, J., Arce, P., Asai, M., Aso, T., Yoshida, H., 2016. Recent developments in GEANT4. Nucl. Instrum. Methods Phys. Res. 835, 186–225. https://doi.org/10.1016/j.nima.2016.06.125.

Bocher, M., Blevis, I.M., Tsukerman, L., Shrem, Y., Kovalski, G., Volokh, L., 2010. A fast cardiac gamma camera with dynamic SPECT capabilities: design, system validation and future potential. Eur. J. Nucl. Med. Mol. Imag. 37 (10), 1887–1902. https://doi.org/10.1007/s00259-010-1488-z.

Breitenmoser, D., Cerutti, F., Butterweck, G., Kasprzak, M.M., Mayer, S., 2023. Emulator-based Bayesian inference on non-proportional scintillation models by compton-edge probing. J. N. C. Nat. Commun. 14 (1), 7790. https://doi.org/10.1038/s41467-023-42574-y.

Brown, J.C., Gerhardt, T.E., Kwon, E., 2023. Risk factors for coronary artery disease. In: StatPearls [Internet]. StatPearls Publishing.

Cano-Ott, D., Tain, J., Gadea, A., Rubio, B., Batist, L., Karny, M., 1999. Monte Carlo simulation of the response of a large NaI (Tl) total absorption spectrometer for β-decay studies. Equipment, A. Nucl. Instrum. Methods Phys. Res. Sect. A Accel. Spectrom. Detect. Assoc. Equip. 430 (2-3), 333–347. https://doi.org/10.1016/S0168-9002(99)00217-X.

Celler, A., 2010. Single photon imaging and instrumentation. J. E. o. S., & Spectrometry 2531–2538. Elsevier Oxford.

Chen, L., Tsui, B.M., Mok, G.S., 2017. Design and evaluation of two multi-pinhole collimators for brain SPECT. J. A. o. n. m. Ann. Nucl. Med. 31 (8), 636–648. https://doi.org/10.1007/s12149-017-1195-y.

Chua, S.C., Ganatra, R.H., Green, D.J., Groves, A.M.J.I., 2006. Nuclear cardiology: myocardial perfusion imaging with SPECT and PET. Imaging 18 (3), 166–177. https://doi.org/10.1259/imaging/20803801.

collaboration, C.-., Lee, S., Adhikari, G., Carlin, N., Cho, J., Choi, J., Ha, C., 2024. Nonproportionality of NaI (Tl) scintillation detector for dark matter search experiments. J. T. E. P. J. C. Eur. Phys. J. C 84 (5), 484. https://doi.org/10.1140/epjc/s10052-024-12770-1.

Deprez, K., Van Holen, R., Vandenberghe, S., 2013. A high resolution SPECT detector based on thin continuous LYSO. J. P. i. M., & Biology Phys. Med. Biol. 59 (1), 153. https://doi.org/10.1088/0031-9155/59/1/153.

Dong, X., Saripan, M.I., Mahmud, R., Mashohor, S., Wang, A., 2018. Characterization of SIEMENS Symbia T SPECT camera in Monte Carlo simulation environment. J. P. J. o. N. M. Pak. J. Nucl. Med. 8 (1). https://doi.org/10.24911/PJNMed.175-1540569779.

Dorbala, S., Ananthasubramaniam, K., Armstrong, I.S., Chareonthaitawee, P., DePuey, E. G., Einstein, A.J., Wells, R.G., 2018. Single Photon Emission Computed Tomography (SPECT) myocardial perfusion imaging guidelines: instrumentation, acquisition, processing, and interpretation. J. Nucl. Cardiol. 25 (5), 1784–1846. https://doi.org/10.1007/s12350-018-1283-y.

Erlandsson, K., Kacperski, K., van Gramberg, D., Hutton, B.F., 2009. Performance evaluation of D-SPECT: a novel SPECT system for nuclear cardiology. Phys. Med. Biol. 54 (9), 2635–2649. https://doi.org/10.1088/0031-9155/54/9/003.

Feng, Y., Kupinski, M.A., Ottensmeyer, M.P., Worstell, W., Tawakol, A., Furenlid, L.R., 2025. Analytical methods for system matrix calculation and spatial resolution evaluation of DC-SPECT system. Biology Phys. Med. Biol. 70 (14), 145031. https://doi.org/10.1088/1361-6560/adedf7.

Gheisari, F., Kamali, M., Liyaghat, M., Atefi, M., Motamedi, A., 2025. Optimizing myocardial perfusion scan quality with SPECT: a hybrid systematic narrative review. J. J. o. R. i. M. S. J. Rev. Med. Sci. 5 (1), 1–11. https://doi.org/10.22034/jrms.2025.498154.1036.

Goulet, M., Archambault, L., Beaulieu, L., Gingras, L., 2013. 3D tomodosimetry using long scintillating fibers: a feasibility study. J. M. P. Med. Phys. 40 (10), 101703. https://doi.org/10.1118/1.4819937.

Gunaratna Mudiyanselage, N., Smith, D., Hobson, P., 2024. Determination of energy resolution for YSO: ce detector modelled with FLUKA code. IEEE Nucl. Sci. Symp. Med. Imaging Conf. (NSS/MIC). https://doi.org/10.1109/NSS/MIC44845.2022.10398959.

Hendrick, R.E., Hendee, W.R., 2008. Breast MRI: fundamentals and technical aspects. J. M. P. Med. Phys. 35 (3), 823–824. https://doi.org/10.1118/1.2840347.

Hutton, B.F., Erlandsson, K., Thielemans, K., 2018. Advances in clinical molecular imaging instrumentation. Clin. Transl. Imaging 6 (1), 31–45. https://doi.org/10.1007/s40336-018-0264-0.

Kaewkhao, J., Limkitjaroenporn, P., Chaiphaksa, W., Kim, H., 2016. Non-proportionality study of CaMoO4 and GAGG: ce scintillation crystals using Compton coincidence technique. J. A. R., & Isotopes Appl. Radiat. Isot. 115, 221–226. https://doi.org/10.1016/j.apradiso.2016.06.030.

Kishimoto, A., Kataoka, J., Taya, T., Tagawa, L., Mochizuki, S., Ohsuka, S., Kawachi, N.J. S.r., 2017. First demonstration of multi-color 3-D in vivo imaging using ultra-compact Compton camera. Sci. Rep. 7 (1), 2110. https://doi.org/10.1038/s41598-017-02377-w.

Lange, K., Carson, R., 1984. EM reconstruction algorithms for emission and transmission tomography. J. J. C. A. T. J. Comput. Assist. Tomogr. 8 (2), 306–316. https://doi.org/10.1097/00004728-198404000-00002.

Leube, J., Claeys, W., Gustafsson, J., Salas-Ramirez, M., Lassmann, M., Koole, M., Tran-Gia, J., 2024. Position dependence of recovery coefficients in 177Lu-SPECT/CT reconstructions–phantom simulations and measurements. J. E. p. EJNMMI Phys. 11 (1), 52. https://doi.org/10.1186/s40658-024-00662-y.

Liang, H., Jan, M., Lin, W., Yu, S., Su, J., Shen, L., 2009. Development of an LYSO based gamma camera for positron and scinti-mammography. J. J. o. I. J. Instrum. 4 (8), P08009. https://doi.org/10.1088/1748-0221/4/08/P08009.

Lois, C., Aguiar, P., Couce, B., Iglesias, A., 2010. Characterization of low energy Lu background on continuous LYSO blocks. IEEE Nucl. Sci. Symp. Med. Imaging Conf. (NSS/MIC). https://doi.org/10.1109/NSSMIC.2010.6036244.

Ma, T., Wei, Q., Lyu, Z., Zhang, D., Zhang, H., Wang, R., He, Z.-X., 2021. Self-collimating SPECT with multi-layer interspaced mosaic detectors. J. I. T. o. M. I. IEEE Trans. Med. Imag. 40 (8), 2152–2169. https://doi.org/10.1109/TMI.2021.3073288.

Ma, T., Zhang, D., Wangi, R., Cheng, L., 2023. Recent advance in SPECT myocardial perfusion imaging and their clinical application values. Med. J. Peking Union Med. Coll. Hosp. 14 (4), 691–697. https://doi.org/10.12290/xhyxzz.2023-0172.

Nakanishi, K., Yamamoto, S., Kataoka, J., 2017. Performance comparison of finely pixelated LYSO-and GAGG-based Si-PM gamma cameras for high resolution SPECT. Nucl. Instrum. Methods Phys. Res. Sect. A Accel. Spectrom. Detect. Assoc. Equip. 872, 107–111. https://doi.org/10.1016/j.nima.2017.08.013. J. N. I., Methods in Physics Research Section A: Accelerators, S., Detectors, & Equipment, A.

Nakano, S., 2016. 4D Reconstruction of Dynamic Studies with the Discovery NM 530c SPECT Camera.

Nishikido, F., Kikuchi, J., Doke, T., Takahashi, H., 2005. Design and simulation study for full size liquid Xe scintillation TOF-PET system. IEEE Nucl. Sci. Symp. Conf. Rec. https://doi.org/10.1109/NSSMIC.2005.1596914, 2005.

Patton, J.A., Slomka, P.J., Germano, G., Berman, D.S., 2007. Recent technologic advances in nuclear cardiology. J. Nucl. Cardiol. 14 (4), 501–513. https://doi.org/10.1016/j.nuclcard.2007.06.003.

Rigaud, G., Hahn, B., 2021. Reconstruction algorithm for 3D Compton scattering imaging with incomplete data. J. I. P. i. S., & Engineering Inverse Probl. Sci. Eng. 29 (7), 967–989. https://doi.org/10.1080/17415977.2020.1815723.

Rodriguez-Molares, A., Rindal, O.M.H., D'Hooge, J., Masoy, S.-E., Austeng, A., Bell, M.A. L., Torp, H., 2020. The generalized contrast-to-noise ratio: a formal definition for lesion detectability. IEEE Trans. Ultrason. Ferroelectrics Freq. Control 67 (4), 745–759. https://doi.org/10.1109/tuffc.2019.2956855.

Roser, J., Hueso-González, F., Ros, A., Llosá, G., 2021. Compton cameras and their applications. In: Radiation Detection Systems. CRC Press, pp. 161–198.

Slomka, P.J., Berman, D.S., Germano, G., 2014. New Cardiac cameras: Single-Photon emission CT and PET. Semin. Nucl. Med. 44 (4), 232–251. https://doi.org/10.1053/j.semnuclmed.2014.04.003.

Valentine, J.D., Rooney, B.D., 1994. Design of a Compton spectrometer experiment for studying scintillator non-linearity and intrinsic energy resolution. J. N. I., Methods in Physics Research Section A: Accelerators, S., Detectors, & Equipment, A. Nucl. Instrum. Methods Phys. Res. Sect. A Accel. Spectrom. Detect. Assoc. Equip. 353 (1-3), 37–40. https://doi.org/10.1016/0168-9002(94)91597-0.

Van Audenhaege, K., Vandenberghe, S., Deprez, K., Vandeghinste, B., Van Holen, R., 2013. Design and simulation of a full-ring multi-lofthole collimator for brain SPECT. J. P. i. M., & Biology Phys. Med. Biol. 58 (18), 6317. https://doi.org/10.1088/0031-9155/58/18/6317.

Vergnaud, L., Badel, J.-N., Giraudet, A.-L., Kryza, D., Mognetti, T., Baudier, T., Sarrut, D., 2023. Performance study of a 360° CZT camera for monitoring 177Lu-PSMA treatment. EJNMMI Phys. 10 (1). https://doi.org/10.1186/s40658-023-00576-1.

Wang, J., Lan, X., Shi, H., Li, S., 2025. A brief report on the results of the 2024 National survey of nuclear medicine conducted by the Chinese society of nuclear medicine. J. J. o. N. M. Society of Nuclear Medicine 66, 684–685.

Wei, Q., Ma, T., Jiang, N., Xu, T., Lyu, Z., Hu, Y., 2020. A side-by-side LYSO/GAGG phoswich detector aiming for SPECT imaging. Equipment, A. Methods Phys. Res. Sect. A-Accel. Spectrom. Dect. Assoc. Equip. 953, 163242. https://doi.org/10.1016/j.nima.2019.163242.

Yan, X., Yao, R., Deng, X., Liu, Y., Wang, S., Ma, T., 2013. Assessment of hybrid rotation-translation scan schemes for in vivo animal SPECT imaging. J. P. i. M., & Biology Phys. Med. Biol. 58 (4), 965. https://doi.org/10.1088/0031-9155/58/4/965.

Yu, J.G., Wang, S., Wu, J., Ma, T.Y., Liu, Y.Q., 2016. Accurate iterative reconstruction in multi-pinhole SPECT based on simulation point source measurement. J. A. E. S., & Technology At. Energy Sci. Technol.. https://doi.org/10.7538/yzk.2016.50.02.0349.

Zeraatkar, N., Kalluri, K.S., Auer, B., Könik, A., Fromme, T.J., Furenlid, L.R., King, M.A., 2020. Investigation of axial and angular sampling in multi-detector pinhole-SPECT brain imaging. J. I. t. o. m. i. IEEE Trans. Med. Imag. 39 (12), 4209–4224. https://doi.org/10.1109/TMI.2020.3015079.

Zhai, J., Li, J.J.P., 2019. Investigation on the sensitivity and FOM of Ag nanoparticles and nanoarrays. Plasmonics 14 (3), 647–652. https://doi.org/10.1007/s11468-018-0842-Z.